An advanced single-stage turbine facility for investigating non-axisymmetric contoured endwalls in the presence of purge flow

Robin R Jones, Oliver J Pountney, Bjorn L Cleton, Liam E Wood, B Deneys J Schreiner, A J Carvalho Figueiredo, James A Scobie, David J Cleaver, Gary D Lock and Carl M Sangan

r.r.jones@bath.ac.uk, o.j.pountney@bath.ac.uk, b.l.cleton@bath.ac.uk, lew37@bath.ac.uk, bdjs20@bath.ac.uk, ajcbsd20@bath.ac.uk, j.a.scobie@bath.ac.uk, d.j.cleaver@bath.ac.uk, g.d.lock@bath.ac.uk, c.m.sangan@bath.ac.uk

Department of Mechanical Engineering
University of Bath
Bath, BA2 7AY
United Kingdom

ABSTRACT

In modern gas turbines, endwall contouring (EWC) is employed to modify the static pressure field downstream of the vanes and minimise the growth of secondary flow structures developed in the blade passage. Purge flow (or egress) from the upstream rim-seal interferes with the mainstream flow, adding to the loss generated in the rotor. Despite this, EWC is typically designed without consideration of mainstream-egress interactions. The performance gains offered by EWC can be reduced, or in the limit eliminated, when purge air is considered. In addition, EWC can result in a reduction in sealing effectiveness across the rim seal. Consequently, industry is pursuing a combined design approach that encompasses the rim-seal, seal-clearance profile and EWC on the rotor endwall.

This paper presents the design of, and preliminary results from a new single-stage axial turbine facility developed to investigate the fundamental fluid dynamics of egress-mainstream flow interactions. To the authors' knowledge this is the only test facility in the world capable of investigating the interaction effects between cavity flows, rim seals and EWC. The design of optical measurement capabilities for future studies, employing volumetric velocimetry and planar laser induced fluorescence are also presented. The fluid-dynamically scaled rig operates at benign pressures and temperatures suited to these

techniques and is modular. The facility enables expedient interchange of EWC (integrated into the rotor bling), blade-fillet and rim-seals geometries.

The measurements presented in this paper include: gas concentration effectiveness and swirl measurements on the stator wall and in the wheel-space core; pressure distributions around the nozzle guide vanes at three different spanwise locations; pitchwise static pressure distributions downstream of the nozzle guide vane at four axial locations on the stator platform.

1 INTRODUCTION

Secondary endwall flows arise from viscous effects at the endwall and the cross-passage pressure gradient and are responsible for a significant proportion (30% to 50%) of the losses for the turbine stage [1]. These losses can be reduced through non-axisymmetric contouring of the endwall. Endwall contouring (EWC) is used to manipulate the secondary flows in the nozzle guide vane (NGV) or rotor blade (RB) passage by modifying the static pressure field close to the hub. The primary aim of EWC is to limit the cross-passage pressure gradient [2]. This serves to reduce the entrainment of crossflow into the passage vortex (the dominant secondary flow feature – see Section 2.1) and thereby limit its impact on stage losses. CFD-based optimization strategies are typically used in the design of contoured endwalls, with reported efficiency gains in the range 0.3% to 1 %, depending on the operating point and loading of the turbine [3-5].

Until recently, contoured endwalls were optimized for the mainstream flow in isolation of ingress and egress through the turbine rim seal. The mixing between the egress and mainstream flows has been shown to modify the secondary flow features that form in the blade passage downstream of the rim seal with an associated impact on stage performance [6]. Only a handful of researchers have studied EWC with egress-mainstream flow interactions, *e.g.* [7, 8]. These studies have shown that stage efficiency improvements

associated with EWC are highly sensitive to purge flow. Regina *et al.* [8] tested EWC optimized in the absence of purge flow with different purge flow rates. Efficiency improvements relative to the baseline cylindrical endwall decreased as purge flow increased, with EWC proving disadvantageous at the highest purge flow rate tested. A clear conclusion from the work was the need to adopt a "combined design of the endwall contouring and the exit geometry of the rim seal" to realise a reduction in aerodynamic stage loss. Consequently, industry is moving towards a combined approach of rim-seal and endwall designs that account for the complex interaction between the purge and mainstream flows. This approach has competing objectives: first, to reduce the aerodynamic losses associated with secondary flows; second, to ensure that any reduction in aerodynamic loss from EWC does not come at the expense of rim seal performance.

The studies cited above and in Section 3 have been conducted in isolation of the wheel-space. This paper presents the design of, and preliminary results from, a new single-stage axial turbine facility designed to study the combined impact of EWC and rim seal design on stage efficiency and ingress. The facility will allow the implementation of state-of-the-art CO_2 planar laser induced florescence (PLIF) and volumetric velocimetry (VV) optical measurement techniques to track egress flow paths and map three-dimensional velocity fields above the rim seal and in the RB passage. The optical measurements will provide insight into the fundamental fluid dynamics of egress-mainstream flow interactions and the effect of these interactions on the secondary flow features. Gas concentration, pressure and swirl measurements in the wheel-space will be used to characterise rim seal performance, enabling the impact of combined EWC and rim seal designs on ingress to be assessed.

Section 2 provides an overview of the fundamental fluid dynamics associated with secondary flows, ingress and egress. Section 3 reviews literature relevant to the topic of

endwall contouring. Section 4 details the design of the test facility. Initial concentration and pressure measurements from the facility are presented in Section 5. Section 6 shows the state-of-the-art optical measurement capabilities for future fluid visualisation studies. Finally, Section 7 gives the primary conclusions of the paper.

2 FLUID DYNAMICS OF SECONDARY FLOWS, INGRESS & EGRESS

2.1 Secondary flows

Detailed discussions on secondary flow features in axial turbines can be found in Langston *et al.* [1], Harvey *et al.* [2], Wood *et al.* [9] and Takeshi *et al.* [10]. Salient points from these discussions are summarised below.

Figure 1 illustrates the stator secondary flow structure and rotor EWC. The boundary layer of the incoming flow rolls up at the leading edge of the blade, forming what is commonly referred to as the horseshoe vortex. The portion of the inlet boundary layer that does not form the horseshoe vortex is deflected across the passage towards the suction surface of the adjacent blade. The endwall separation line marks the point at which the inlet boundary layer separates from the surface of the endwall. The endwall crossflow, which is driven by the cross-passage pressure gradient, forms a new boundary layer downstream of this separation line.

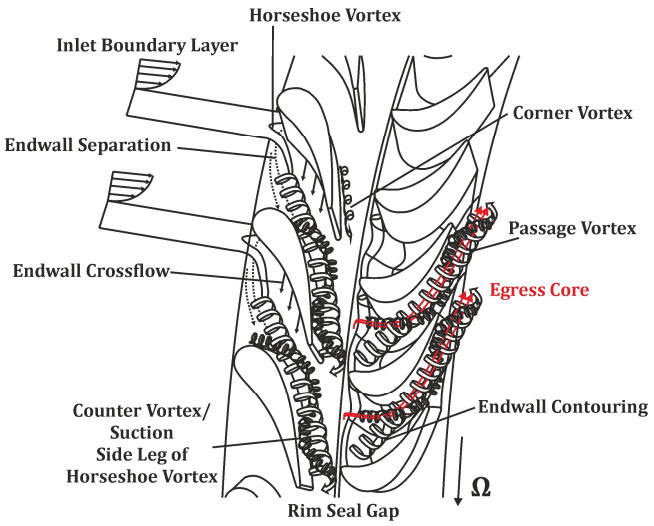

Figure 1 Stator secondary flows and endwall contouring. Adapted from [9].

Loss mechanisms related to the endwall are complex; a comprehensive discussion is provided by [11]. A significant proportion of the total endwall loss comes from entropy generation in the endwall boundary layers, upstream, within and downstream of the blade row. Also important is the increase in entropy resulting from the decay of secondary kinetic energy (SKE – the component of kinetic energy normal to the direction of the primary flow). The streamwise vorticity of the passage, counter and corner vortices gives rise to SKE. Dissipation within the cores of these vortices is a significant contributor to the decay of SKE in the passage. EWC aims to serve two purposes: first, to reduce the level of entrainment of crossflow into (and thus growth of) the passage vortex, bringing about a reduction in the generation of entropy associated with dissipation of SKE; second, to reduce the skew of the inlet and endwall crossflow boundary layers, decreasing viscous losses.

2.2 Ingress and egress

Ingress refers to the inflow of hot gas from the annulus into the rotor-stator wheel-space cavity through the peripheral rim seal gap; a detailed review of research into this topic is provided by Scobie *et al.* [12]. The NGVs and RBs produce a non-axisymmetric circumferential pressure profile above the rim seal, resulting in ingress in regions where the

pressure in the annulus exceeds the pressure in the wheel-space. Ingress is undesirable as it results in heating of the highly stressed rotating disc. Hence, purge flow is used to pressurise the wheel-space, sealing against ingress. Complex rim seal designs are employed to limit the amount of purge flow required for this purpose. The egress discharges through the turbine rim seal at locations where the circumferential pressure in the annulus is less than that in the wheel-space.

Figure 2 shows a simplified schematic of the flow structure of a rotor-stator system with ingress and egress. The velocity and concentration boundary layers on the surfaces of the two discs are included for the case where purge flow, with swirl, is supplied to the system at low radius. Scobie *et al.* [12] provide a detailed discussion of the fluid dynamics within the wheelspace. The geometry shown in Fig. 2 is a generic version of a typical double-seal with a chute arrangement for the outer seal; this is the geometry used in the test facility for the results presented in this paper.

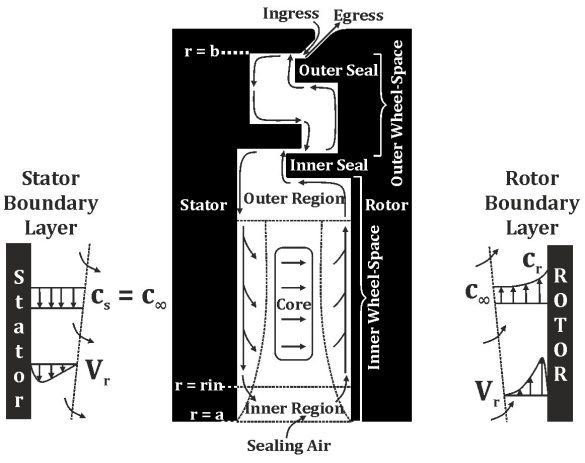

Figure 2 Schematic of the flow structure in a rotor-stator system. Stator and rotor velocity and concentration boundary layers are shown left and right respectively. Adapted from [12].

The wheel-space dimensions and turbulent flow parameter in most engine cavities are such that Bachelor-type flow is formed in the inner wheel-space. This type of flow is characterised by boundary layers on the rotor and stator that are separated by an inviscid core of fluid rotating at less than the disc speed. In the core region, the radial velocity component is zero and the axial and tangential velocity components remain constant in the axial direction (this is in accordance with the Taylor-Proudman theorem). It follows that radial flow in the wheel-space is restricted to the disc boundary layers: fluid flows radially outward on the rotor and radially inward on the stator. The inner and outer regions feed the stator and rotor boundary layers respectively. The rotor boundary layer grows with radius owing to the entrainment of fluid from the inner region (which includes the supplied purge flow) and the core. The flow of fluid from the core into the rotor boundary layer is balanced by flow from the stator boundary layer into and axially across the core. As a result, the thickness of the stator boundary layer reduces at lower radius.

The flow in the outer wheel-space region is characterised by intense mixing of the ingress and egress flows in a small region close to the outer seal. This mixed out swirling fluid flows radially inwards on the stator and radially outwards on the rotor. The egress flow is ejected from the rim seal on the rotor-side, subsequently mixing with the mainstream flow.

3 LITERATURE REVIEW

Section 3.1 provides a brief overview of the previous research into EWC and egress-mainflow interactions. The purpose of this overview is not to provide an extensive review of previous work, but rather summarise the development in understanding that has led to the current opinion that contoured endwalls and rim seals must be designed in combination. Research into egress-mainstream interactions with EWC is relatively sparse, as is the impact of EWC on ingress levels. The test facility presented in this paper aims to provide much

needed research into these areas. Section 3.2 provides an overview of the CO_2 PLIF and VV measurement techniques that can be used to investigate secondary flows in the annulus.

3.1 Endwall contouring and egress-mainstream flow interactions

Several researchers (*e.g.* [6, 13-15]) have investigated the effect of egress on secondary flow formation without EWC, with the general conclusion being that the strength and spanwise penetration of the secondary flows tend to increase as the egress flow rate is increased. Ong *et al.* [15] suggested that this is caused by the negative incidence associated with the egress flow (the egress flow exits the rim seal with lower momentum and swirl than the mainstream flow, modifying the velocity triangle near to the endwall). In addition to increased secondary flow losses, the egress-mainstream flow interaction also increases viscous mixing losses.

Schüpbach *et al.* [7] were the first to investigate the effect of egress flow on the performance of an endwall profiled turbine. The authors tested two endwall designs (employing torque measurements and fast response aerodynamic probes), both of which were optimised without egress flow; the study was performed in conjunction with time-resolved computational simulations. Their results showed that stage total-to-total efficiency improvements offered by EWC relative to the cylindrical baseline reduced as egress flow rates increased. This finding was supported by the results of a subsequent similar study by Regina *et al.* [8], with EWC even proving disadvantageous at the highest purge flow rate tested. Both studies reached the same conclusion: it is essential to consider egress flow in the design of contoured endwalls if stage efficiency benefits from EWC are to be realised. Regina *et al.* also recommended combining the design of the endwall and rim seal so that the radial and tangential velocity components of the egress flow can be controlled to limit the enhancement of the secondary flow and mixing losses associated with the egress-mainstream flow interaction. This combined approach must also consider the impact of EWC

on the performance of the rim seal. It is essential that stage efficiency improvements from EWC are not offset by increased ingress; which would necessitate additional purge.

3.2 Optical measurement techniques

The test facility is designed to accommodate two state-of-the-art optical measurements techniques: CO_2 PLIF and VV. Neither of these techniques have previously been used in a rotating environment; however, several researchers have successfully used other optical measurement technologies in turbomachinery applications (*e.g.* particle image velocimetry; see [16-20]). The methods of seeding, laser-delivery and optical access employed in these previous studies provide useful design guidelines for using CO_2 PLIF and VV in the new facility. These methods will be outlined after a brief introduction to these techniques.

PLIF is a technique that uses a laser sheet to excite molecular transitions of gas species in fluid flows and is commonly used to study combustion [21, 22]. These transitions result in the emission of photons (*i.e.* fluorescence) that can be captured using an appropriate image sensor. The intensity of the fluorescence is proportional to the tracer concentration. Typically, the tracer is a florescent dye, such as fluorescein or Rhodamine [23]; however, these are toxic and must be injected (and appropriately mixed out) in the flow. In contrast, CO_2 is naturally used in many experimental situations, for example as the cooling flow in film cooling studies. The use of CO_2 as a PLIF tracer gas was first demonstrated by Kirby *et al.* [21, 22]; it has since been used by Zetterberg *et al*. [24] to measure CO_2 concentration directly above a catalyst surface. The use of CO_2 PLIF in turbomachinery applications has not yet been demonstrated; however, PLIF with a Rhodamine tracer has been successfully used in a recent study of endwall film cooling [25]. The test rig presented in this paper is designed to use CO_2 PLIF to measure the local concentration of CO_2-seeded egress flow as

it mixes with the mainstream flow above the rim seal and propagates through the downstream RB passage.

VV is a particle tracking technique that provides measurements of the instantaneous three-component velocity field in a fluid volume. The flow is seeded with trace particles using a droplet generator. These trace particles are illuminated at two instances, separated by a known time-step, using a pulsed laser to illuminate a volume of particles; at each pulse, three CCD cameras capture a frame of the flow. The six frames (three at the first laser pulse and three at the second laser pulse) are then processed using the method described in Carvalho Figueiredo *et al*. [26]. The method computes the displacement of particles between the two laser pulses and subsequently computes the velocity with the known/measured time-step. This involves particle identification in each frame, particle matching to obtain the particles' 3D coordinates at each pulse and velocity processing. The particle tracking algorithm detailed in Stellmacher and Obermayer [27] has been robustly used with VV. The output comprises velocity vectors at the coordinate location of each particle. The capture process described above is repeated multiple times. Gaussian weighted velocity averaging is subsequently used to generate velocity vectors in a structured grid. Carvalho Figueiredo *et al*. [26] are the only researchers to have published VV measurements in the field of turbomachinery, successfully tracking the flow path and circulation of film cooling kidney vortices. VV will be used in the new test facility to capture the interaction between the egress and mainstream flows and ascertain the strength of the secondary flow features in the RB passage. This will provide insight into the fundamental fluid dynamics and useful data for validation of CFD.

Woisetschläger and Göttlich [28] provide an in-depth discussion on the application of PIV to the study of turbomachinery fluid dynamics. CO_2 PLIF and VV require the same basic configuration as standard PIV techniques: a system for seeding the flow with trace

particles; a means of introducing the laser to the test region; and windows to provide a view of the illuminated flow to the cameras.

The PLIF system is being used to study the mixing of two flows and so one of the flows (the purge flow) must be supplied with a known mixed-out concentration of CO_2. Whereas the VV systems requires seeding of both purge and mainstream flows.

The regions of interest in most turbomachinery applications are difficult to access for both the laser and camera owing to the closed and confined environment, and so researchers have had to develop novel approaches to address this problem. Woisetschläger and Göttlich [28] suggest that the most practical method of introducing the laser sheet to the test region is through light-sheet probes (referred to as borescopes herein). Some researchers have installed their borescopes within NGVs to avoid disturbances to the flow. For example, Chana *et al.* [17] delivered laser sheets to their working section through borescopes in NGVs fitted with transmissive windows. The turning of the RBs makes it virtually impossible to illuminate the entire RB passage with a single borescope, and so multiple borescopes are used simultaneously to provide greater coverage. Ceyhan *et al.* [29] used two borescopes to illuminate the RB passage in their experiments: one installed upstream of a transmissive NGV row and one installed downstream of their RB row.

The illuminated region is typically viewed through windows in the casing for a direct view of the test region. The curvature of the casing is matched on the inner surface of the window, with spatial calibrations required to account for refraction. Carvalho Figueiredo *et al*. [26] used borosilicate glass windows in their VV experiments. The wetted surface of the glass was coated with an oleophobic coating to prevent accumulation of oil droplets. In the CO_2 PLIF experiments, the CO_2 particles fluoresce in the infrared; hence, windows that transmit infrared radiation are required. Zetterberg *et al.* [24] used Calcium Fluoride windows; Germanium, Silicon and Sapphire are suitable alternatives.

CO_2 PLIF and VV are slow acquisition systems (~10Hz). The fluid dynamics associated with egress-mainstream flow interaction and secondary flow development is highly unsteady. Woisetschläger and Göttlich [28] suggest using ensemble-averaged PIV measurements at different rotor-stator positions. Data will be acquired for a set number of relative RB-NGV positions over a NGV pitch (*i.e.* phase-locked) and then averaged over a statistically significant number of repetitions. These ensemble-averaged results can be animated to illustrate the periodic flow field.

4 EXPERIMENTAL FACILITY

This section presents the design, measurement capabilities and operating conditions of the new one-stage axial turbine facility at the University of Bath: the Large Annulus Rig (LAR). This facility has been designed to provide expedient optical access for state of the art borescopic instruments. These instruments will reveal the fundamental fluid dynamics which govern the mainstream-egress interactions and other secondary flow features through the turbine. In addition, the facility has been designed to offer pressure and concentration measurements inside the wheel-space and the annulus.

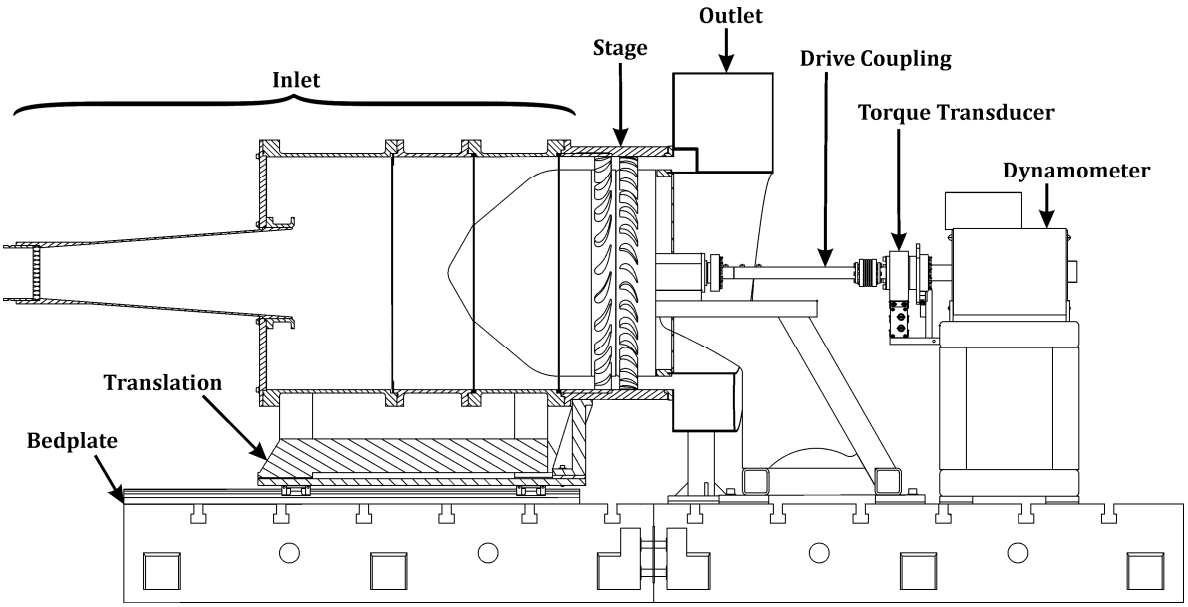

Figure 3 Section view of the Large Annulus Rig (LAR).

The rotor features turned blades and can provide a maximum $Re_\phi = 7.2 \times 10^5$ and a vane exit Mach number of M = 0.14 at a flow coefficient of $C_F = 0.38$. Although these conditions do not approach the Reynolds numbers experienced in real gas turbine engines ($Re_\phi > 10^7$), the LAR was designed to match typical engine values of turbulent flow parameter, λ_T, in the wheelspace which, in modern engines, is usually less than 0.22. For fully sealed conditions ($\Phi_0 \sim 0.15$), the turbulent flow parameter was $\lambda_T \sim 0.1$ in the LAR. Details of all instrumentation, including associated measurement uncertainty, are given in the Appendix.

The rotor (which includes the EWC integrated as a single bling), stator and rim seals are all modular. Once the inlet is translated to disengage the stator from the rotor, the user can easily access and remove these components and replace them with other desirable test geometries.

Torque and 5-hole probe measurement capabilities have also been incorporated into the design to ascertain the stage efficiency; these capabilities and measurements are beyond the scope of this article and will feature in future publications.

4.1 Test rig

Figure 3 presents the experimental facility. An Atlas Copco (model ZS 160+ VSD) compressor provides the main annulus flow of the turbine. The compressor is capable of sustaining a mass flow rate of 1.5 kg/s of atmospheric air at a maximum working gauge pressure of 1.2 bar. Main flow is delivered to the experimental facility through a 6 inch pipeline (shown at the extreme left of Fig. 3). The mass flow rate is measured with a FlatTrak 780S thermal mass flow meter provided by SIERRA instruments.

Thermostatic control of the annulus flow is achieved with a dual-line water cooled heat exchanger; a k-type thermocouple measures the main flow temperature at the exit of the heat exchanger. In this study, the annulus flow is maintained at 25 °C by a PID controller.

The facility is centrally controlled (with data logging) by a CADET V14 system with CP 128 I/O cards provided by Sierra CP.

4.2 Inlet design

Axisymmetric flow is supplied to the annulus by the inlet section of the facility (see Fig. 3). The design of the inlet was based on a similar test facility designed in collaboration with Siemens Industrial Turbomachinery Ltd. and consistent with other designs in the open literature (*e.g.* [30]). Main flow enters the inlet section via a conical diffuser with an expansion angle of 4.3° to the longitudinal axis [31]. A 20 mm thick aluminium honeycomb insert with 5 mm circumradius straightens the supplied flow at the anterior aspect of the diffuser. The inlet drum is Ø704 mm internally; this matches the external diameter of the turbine annulus. There are two baffle plates which generate a pressure drop within the inlet drum; these were found to promote uniform annulus flow. The baffle plates have Ø9 mm circular pores in a triangular mosaic pattern with equilateral side length 11 mm and an open area ratio of 60%; the thickness is 3 mm. A nose-cone within the inlet section forces the main flow to contract into the turbine annulus. The nose cone encases the purge feed line to the wheel-space and pneumatic tubing to the pressure taps.

The design of the inlet was iteratively developed and simulated using CFD. Figure 4 shows the five most significant design iterations, shown chronologically from (a) to (e). A grid sensitivity study was carried out using three grid levels and a Richardson extrapolation for the pressure drop in lieu of experimental data. Three sector sizes were tested, 10°, 30°, and 45°. 30° was selected because it matches the minimum sector for a 24:36 NGV-to-RB count; 10° yielded poor quality unstructured cells towards the central axis; it afforded a 30% reduction in domain volume compared to the 45° sector with no discernible change to the flow field.

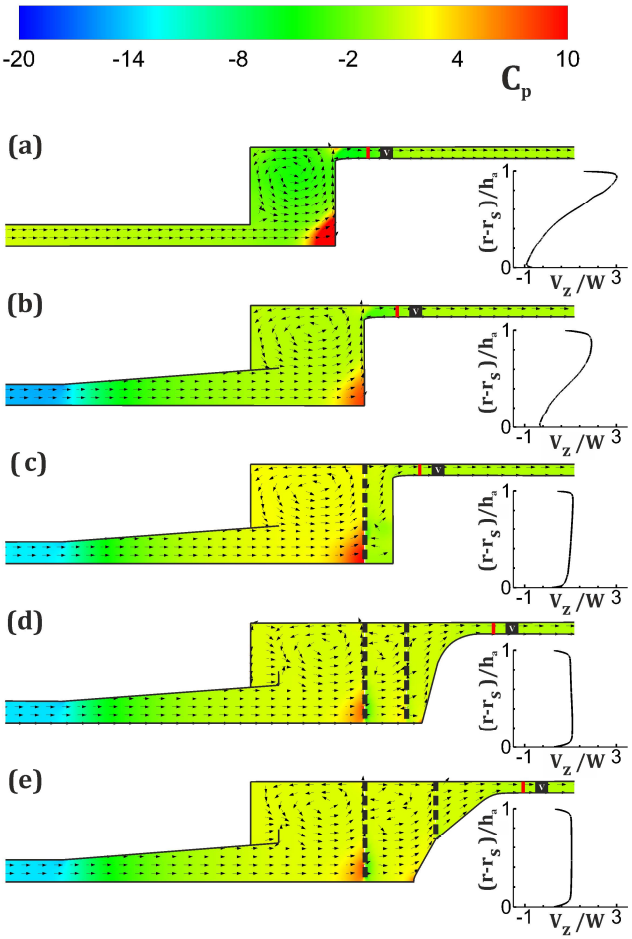

Figure 4 Five iterations of the inlet design with CFD results extracted from the mid-section of the model. Colour maps – planar distribution of C_P; arrows – planar unitary flow vectors; plot inserts – radial distribution of axial velocity along the red line.

Computational simulations of the inlet were performed in ANSYS Fluent v15.0 with a shear stress transport (SST) turbulence model. The nondimensional first cell height was set to $y^+ \geq 11$. A refinement ratio of 1.4 was used between grid levels, as per [32]. The computational model exploited the axisymmetric nature of the inlet volume and the domain was hence modelled as a sector rather than a full cylinder. An unstructured grid was employed to circumvent infinitesimally small cells at the rotational axis.

Figure 4e shows the final inlet design. Three criteria were considered paramount in the design: radial distribution of axial velocity one axial NGV chord upstream of the NGV

leading edge (indicated by the red lines in Fig. 4, with distributions shown on the RHS), total pressure loss and overall length. Other criteria, such as total pressure distribution, flow angle distribution and peak tangential velocity were also considered. For brevity, the discussion focuses on the radial distribution of axial velocity.

The first design (a settling chamber, Fig. 4a) demonstrated recirculation near the NGV leading edge; the radial distribution of velocity was considered to be inadequate. The diffuser (shown in Fig. 4b) was introduced and achieves an exit jet velocity one third of that entering the diffuser. A single baffle (shown in Fig. 4c) with a blockage ratio of ≈ 50% was found to provide another improvement to the distribution of velocity. The holes were Ø20 mm, keeping the total hole count low in order to reduce computational effort. Increasing the length of the settling chamber facilitated the introduction of a second baffle plate (shown in Fig. 4d); the baffle plates' open area was increased to ≈ 60%. This was found to further improve the uniformity of the radial distribution of axial velocity. The introduction of a second baffle with increased open area resulted in a reduction in total pressure drop by ≈ 10%. An iterative, combined design approach was pursued with two baffle plates and a shaped conical nose. The final design employed differing nose cone angles upstream and downstream of the second baffle plate which was tuned to yield the accepted final radial distribution of axial velocity (see Fig. 4e).

The inlet design was assessed experimentally with Pitot-tube measurements of the radial distribution of axial velocity. Figure 5 shows the radial distribution of axial velocity (a) and turbulence (b) one axial NGV chord upstream of the NGV leading edge. The CFD inlet design study was performed without a turbulence grid. Figure 5a shows that, with the exception of the boundary layer regions, the deviation of experimental result from the CFD prediction is less than 10%. The mass flow computed from the integrated velocity profile differed from the thermal mass flow meter reading by less than 1.8%.

Turbulence is induced 100 mm upstream of the leading edge of the NGVs using a turbulence grid. The design is a quasi-axisymmetric diamond hole grid based on [33] and can be viewed in Fig. 5.

Figure 5a compares the CFD results (which does not include a turbulence grid) with the velocity measured with a radially traversing Pitot probe; both with and without the turbulence grid. The addition of the turbulence grid modifies the radial distribution of axial velocity. However, with the exception of $(r\text{-}r_s)/h_a < 0.2$, the distribution still deviates from the CFD by less than 10%. Figure 5b shows the radial distribution of turbulence measured using a boundary layer hotwire probe (TSI model 1218-20) and a DISA 56C16 Wheatstone bridge. Hotwire measurements were taken from the annulus hub to the mid-span. The turbulent boundary layer at the hub was found to be ≈ 20% of the annulus span. The turbulence level, σ, was measured to be uniform; ≈ 5% in the region $(r\text{-}r_s)/h_a = 0.2$ to 0.5.

4.3 Turbine stage and instrumentation

The inlet and stator are axially traversable on linear guide rails to allow access to the turbine stage. Access to the instrumentation on the stator is achieved by opening the inlet drum, the anterior baffle plate and the nose cone.

12 static pressure taps are circumferentially distributed one NGV axial chord length upstream of the NGVs through the outer casing of the annulus. Pressure measurements revealed a standard deviation of less than 0.5% of the average static pressure circumferentially. The annulus height is 40 mm, providing a hub-to-tip radius ratio of ≈ 0.89. A Pitot tube, which can traverse the full height of the annulus, is used to measure an inlet boundary condition for CFD modelling.

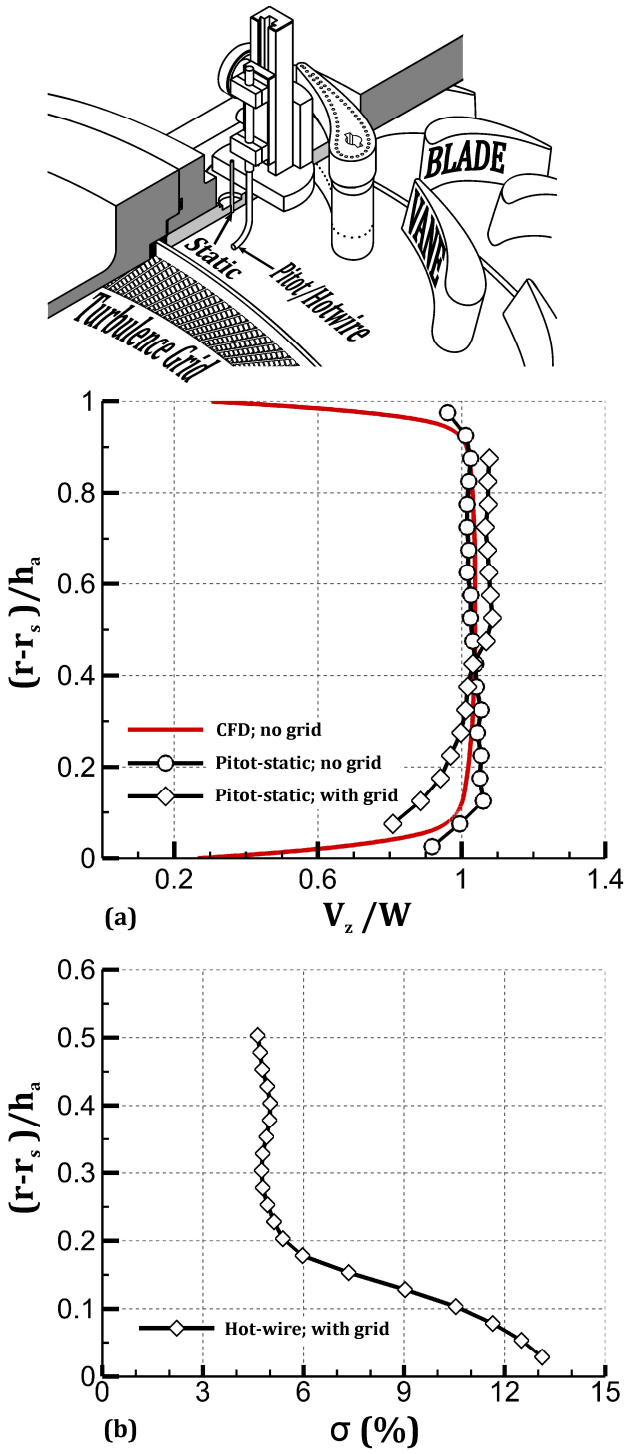

Figure 5 a) Radial distribution of axial velocity at the inlet of the annulus with and without the turbulence grid. b) Radial distribution of turbulence intensity in the annulus with the turbulence grid.

There are 24 NGVs and 36 turned RBs with constant profile across their span and constant 3.5 mm radius fillets at the hub. The profile sections are based on the near hub section design of a modern Siemens industrial gas turbine HP stage. The NGVs have an axial chord length of 50 mm and a span of 40 mm. The RBs have an axial chord length of 54 mm and the same root fillet radius; they have a span of 39.5 mm to provide a 0.5 mm tip-shroud clearance. The vane exit angle was 74°. The relative blade inlet angle was 33°; the blade metal angle was 104°. The stator and rotor were machined as single blings from aluminium; the blings are then fitted to stator and rotor disks, respectively.

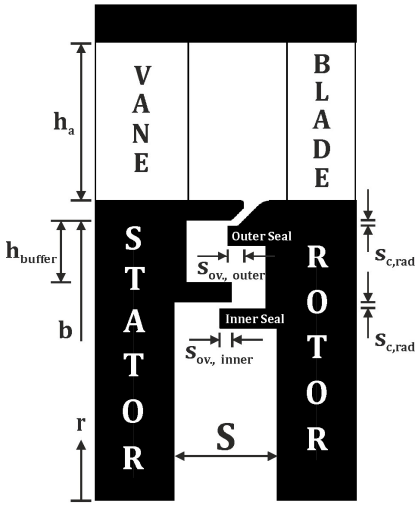

Figure 6 Geometry of the baseline rim seal.

EWC can be machined as part of additional rotor blings, which are interchangeable and relatively inexpensive to manufacture. Wood *et al.* [9] present the EWC design method to be employed in future experiments. The cylindrical rotor and stator hub radius is 312 mm. A double-clearance chute seal (see Fig. 6) was chosen as the baseline rim seal geometry; the geometric parameters of the rim seal are summarised in Table 1.

Parameter	Dimension (mm)
h_a	40
$r_{a,min}$	312
$r_{a,max}$	352
h_{buffer}	16
b	307
S	26
$s_{c,chute}$	2.1
$s_{c,rad}$	1.5
$s_{ov.,outer}$	4
$s_{ov.,inner}$	3

Table 1 Geometric parameters.

The rotor can be driven to a maximum speed of 1500 rpm by a 34 kW asynchronous dynamometer which also absorbs the power generated by the turbine. Rotor torque measurements can be measured using a T12 torque transducer provided by HBM.

At the posterior aspect of the turbine, the exhaust flow is collected by an outlet volute. The rotor hub continues downstream of the RB trailing edge for one RB chord, followed by a 2 mm axial gap between the rotor and stationary volute. Circumferential skew in the exhaust static pressure was mitigated by azimuthal expansion of the volute cross-section in direct proportion to the sector area of the annulus. Nine static pressure taps were distributed circumferentially downstream of the rotor by 30° intervals; there is an arc-segment with missing pressure taps on the optical instrumentation section of the casing. Pressure measurements revealed a standard deviation of 1.5% of the average static pressure circumferentially downstream of the rotor. This deviation was largely due to the residual skew from the volute.

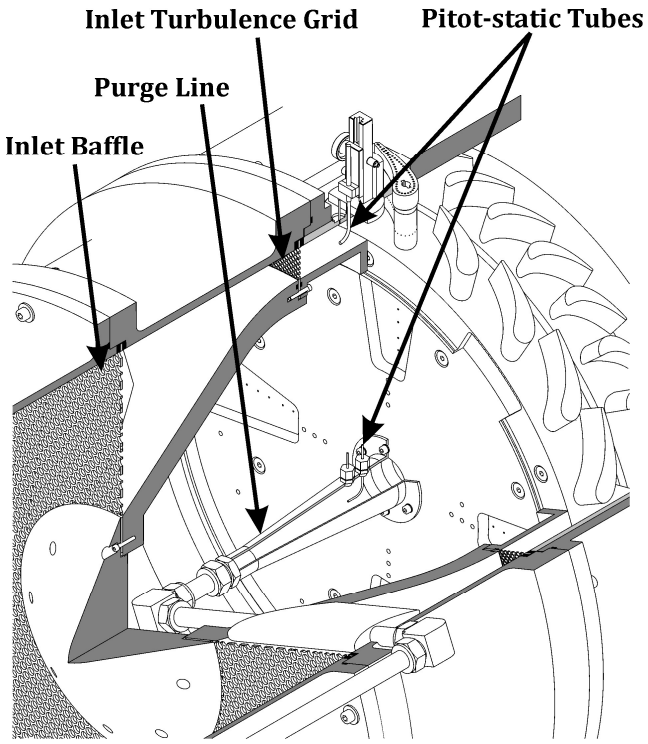

Figure 7 Sectioned view of the large annulus rig showing inside the nose cone cavity.

Purge flow is introduced to the wheel-space through the bore of the stator. Ø18 mm steel tubing encases the purge line and passes directly through the inlet inside aerodynamically-profiled support struts. Figure 7 shows a sectioned view of the purge supply and inlet flow measurement locations. The wheel-space can be purged with a controllable blend of up to 100 % CO_2; the maximum flow rate of CO_2 is ≈ 0.06 kg/s. Mixing of the gas species takes place more than 10 meters (> 400D) upstream of the stator. Hence, the purge flow is expected to be fully mixed (see [34]). The mass flow rates of CO_2 and compressed air are independently controlled with thermal mass-flow controllers. The temperature of the combined purge gas is measured using a k-type thermocouple in the supply line; the static and total pressure is measured at the inlet to the wheel-space (see Fig. 7). The viscosity of the purge flow was calculated using [35].

4.4 Operating Conditions

Table 2 shows the nominal operating conditions of the LAR. The experiments were performed at two disc speeds to confirm Reynolds number independence over the range tested.

Parameters	Disc Speed (RPM)	
	900	1100
Rotational Reynolds Number, $\mathbf{Re}_{\phi}$	5.9×10^5	7.2×10^5
Axial Reynolds Number, $\mathbf{Re}_{w}$	2.2×10^5	2.8×10^5
Flow Coefficient, C_F	0.38	
Vane exit Mach Number, **M**	0.12	0.14

Table 2 Operating conditions

4.5 Instrumentation

This section describes the *non-optical* instrumentation installed into the annulus and wheel-space of the LAR; *optical* measurement capabilities are considered separately in Section 6.

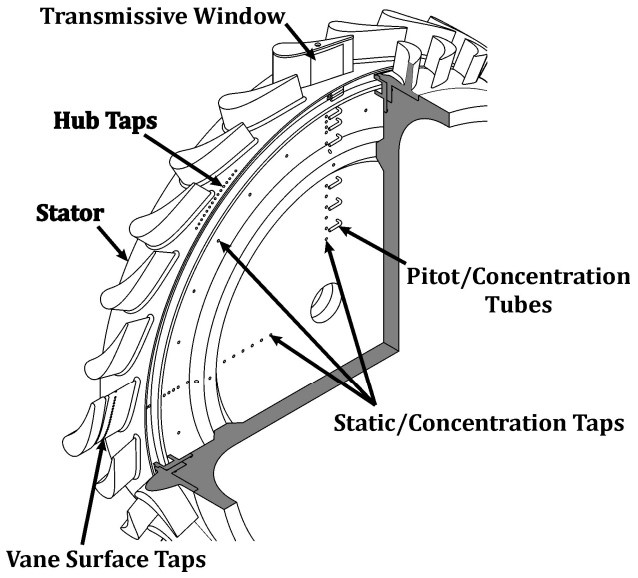

Figure 8 Annulus and wheel-space instrumentation.

Figure 8 shows the stator half of the stage, identifying the pressure and concentration taps. Four of the NGVs are independently manufactured, detachable components: one of which is intended for borescopic optical access and the remaining three are each furnished with 48 pressure taps, at 20%, 50% and 90% of span. These components were additive manufactured using stereolithography. The NGV components were quality checked using a coordinate measurement machine; the deviation of the manufacturing from the nominal surface was less than 50 μm from the surface normal. The surface roughness of the 3D printed NGVs was compared to a sample of a side milled aluminium surface using a Renishaw surface roughness white light interferometer probe. The roughness was found to be $R_a = 4.2 \pm 0.2$ μm which is comparable to an aluminium surface machined in the same manner as the blings ($R_a \sim 5$ μm).

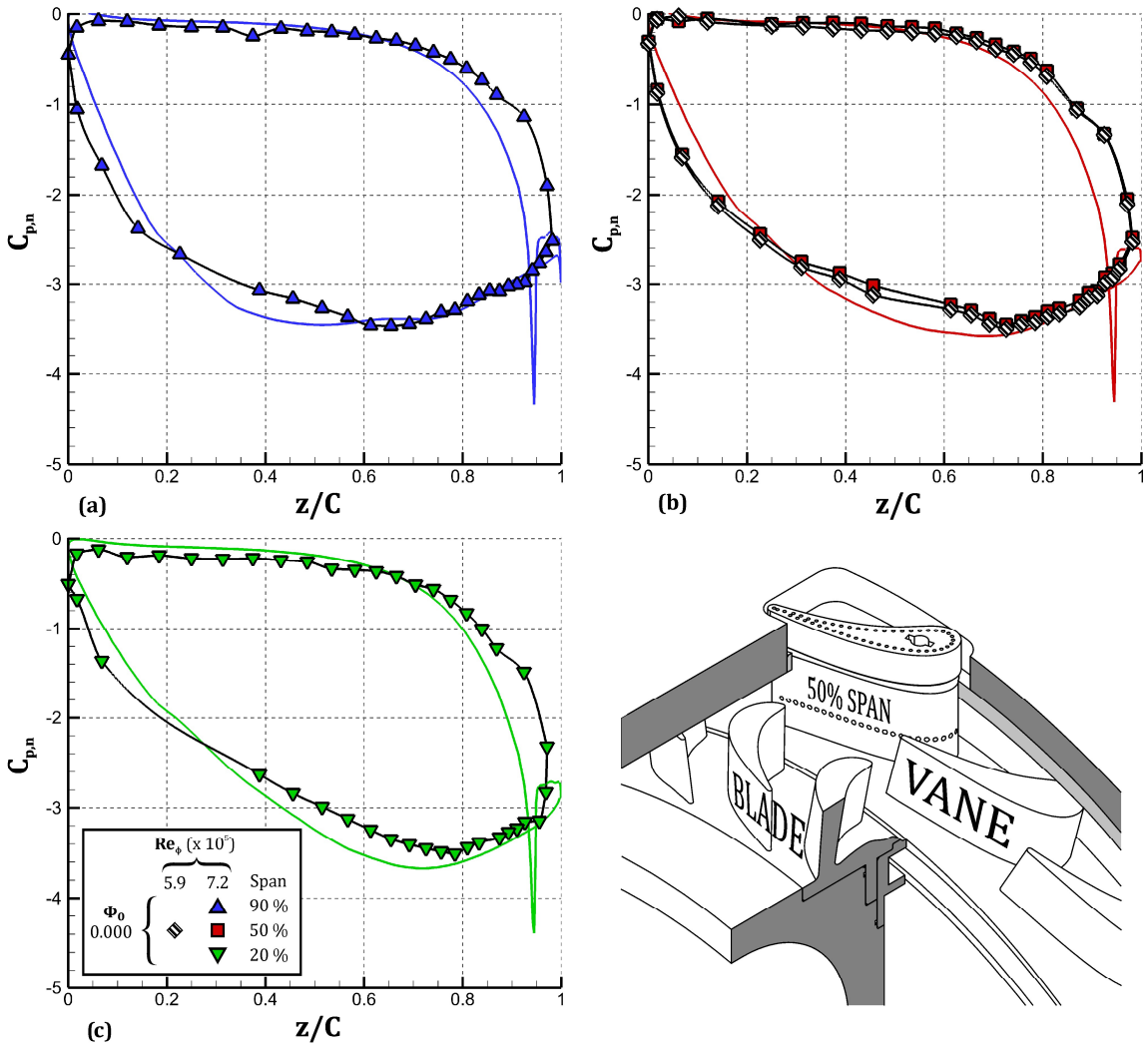

Figure 9 $C_{p,n}$ distribution on stator vanes at three spanwise locations (a, b and c); solid lines are CFD; b) Effect of Re_ϕ on axial distribution of $C_{p,n}$ over the nozzle guide vane taps at 50 % span; $C_F = 0.38$; $\Phi_0 = 0$.

The wheel-space is instrumented with sets of static pressure taps which cover four radial seams (separated by 90° from one another). There are also 12 static taps distributed over the complete circumference at $r/b = 0.825$. The standard deviation of the wheel-space static pressure was less 0.1% of the average static pressure circumferentially. In addition, there is a single set of Pitot tubes which extend $z/S = 0.19$ into the core of the wheel-space from the stator surface (see Fig. 8).

All steady pressure measurements were taken using two, 48-channel, Scanivalves fitted with differential pressure transducers (see Appendix). Ideal gas laws were used to compute the density of annulus and purge flow.

The concentration of CO_2 in any given location was measured using a multi-gas analyser (model: 9120MG) from Signal Group. Sampling taps were multiplexed via a bespoke 20 point sample selector also provided by Signal Group.

Ingestion of mainstream fluid into the wheel-space can be inferred by supplying the purge and mainstream gas with known concentrations of CO_2 and measuring the distribution of effectiveness. Typically, the purge flow supplied to the wheel-space is expressed as the nondimensional sealing flow parameter:

$$\Phi_0 = \frac{U}{\Omega b} \tag{4.1}$$

where U is the bulk mean radial seal velocity. Effectiveness is defined as:

$$\varepsilon = 1 - \frac{\dot{m}_i}{\dot{m}_e} = \frac{\dot{m}_0}{\dot{m}_0 + \dot{m}_i} \tag{4.2}$$

Prior to entering the wheel-space, CO_2 and air are blended to form the superposed flow. The concentration of CO_2 can be varied from 0.04% (atmospheric air) to 100%. The concentration effectiveness is:

$$\varepsilon_c = \frac{c_s^* - c_a^*}{c_0^* - c_a^*} \tag{4.3}$$

where

$$c_s^* = \frac{\rho_{CO2}}{\rho_{air} \cdot (1 - c_s) + \rho_{CO2} \cdot c_s} \cdot c_s \tag{4.4}$$

$$c_a^* = \frac{\rho_{CO2}}{\rho_{air} \cdot (1 - c_a) + \rho_{CO2} \cdot c_a} \cdot c_a \tag{4.5}$$

and

$$c_0^* = \frac{\rho_{CO2}}{\rho_{air} \cdot (1 - c_0) + \rho_{CO2} \cdot c_0} \cdot c_0 \tag{4.6}$$

where c^* denotes mass based concentration and c denotes concentration by volume as measured by the gas analyser.

The mainstream gas is ambient air; CO_2 concentration, c_a, is measured one axial chord upstream of the leading-edge of the NGV. The concentration effectiveness within the wheel-space, c_s, is measured through the stator wall static taps and pitot tubes (see Fig. 8).

5 PERFORMANCE OF THE TEST RIG

This section presents fluid dynamic measurements in the annulus and wheel-space, concluding with the effectiveness of the rim-seal. Predictions from a supporting CFD study are included for comparison. With the exception of Section 5.2, the nature of the results are comparable to those presented in [36].

5.1 Computational simulations

The CFD data presented for comparison was generated using ANSYS CFX. While other turbulence models were tested, the k-ω SST model was used in conjunction with the Kato-Launder production limiter and reattachment modification. No transition models were used. A more detailed description of the numerical simulations are reported in [37], including details of the time-marching calculations; a brief summary of the modelling approach is included here for completeness.

A 30° sector of the rig was modelled, taking advantage of the 24 NGV to 36 RB periodicity. This 2 NGV to 3 RB sector included a stub wheel-space below the annulus, accurately replicating the geometry above $r/b = 0.936$. The domain extended one axial chord upstream of the NGV leading edge and the same downstream of the RB trailing edge.

Grid convergence was shown for velocity profiles and pressure distributions using mixing plane calculations of the stage. This was conducted for three grid levels, with a refinement ratio of 1.4 in each ordinate direction. The final grid selected for generation of computational data contained 1.5 million cells per RB passage. Industrial meshing best practice was adopted for the annulus ($y^+ \leq 10$), while the wheel-space resolution was increased to $y^+ \leq 1$ throughout.

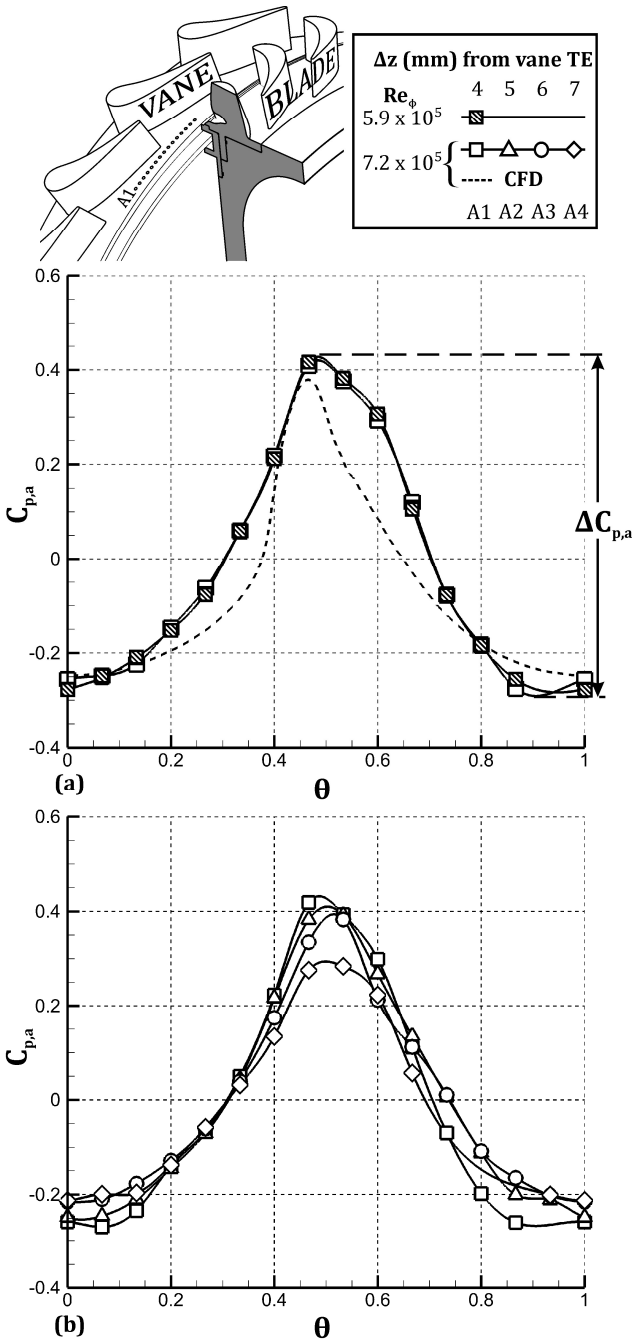

Figure 10 Distribution of $C_{p,a}$ on the stator hub over one vane pitch; a) Effect of Re$_\phi$ 4 mm axially downstream of the vane trailing edge (A1); b) distribution of $C_{p,a}$ at four axial locations from 4 mm to 7 mm downstream of the vane trailing edge (A1 to A4); C_F = 0.38; Φ_0 = 0.

Two domain inlets exist (depending on the run conditions): main gas path, modelled using the experimental velocity profile data (presented in Fig. 5), and the purge inlet, modelled using additional CFD velocity profile data. No purge was introduced in the

simulations presented here. The domain was split into stationary and rotating sections, with a generalised grid interface located upstream of the seal region, isolating the complex interaction between main gas and egress flows from the domain interface.

5.2 Stator vane pressure distributions

Three of the NGVs are detachable components, each furnished with 48 pressure taps at a constant span of 20%, 50% and 90%. Figure 9 shows the axial distribution of $C_{p,n}$ over the NGVs with zero wheel-space purge. Experimental results and CFD are compared in (a), (b) and (c) respectively for the three span-wise positions. Both experiment and CFD demonstrate greater airfoil loading towards the NGV tip relative to the NGV root; this is to be expected with an absence of twist and stack in the NGV profile.

The rotational Reynolds number with constant flow coefficient and zero purge was found to have a negligible effect on the axial distribution of $C_{p,n}$ (Fig. 9b). The effect of purge up to Φ_{min} was also negligible (not presented).

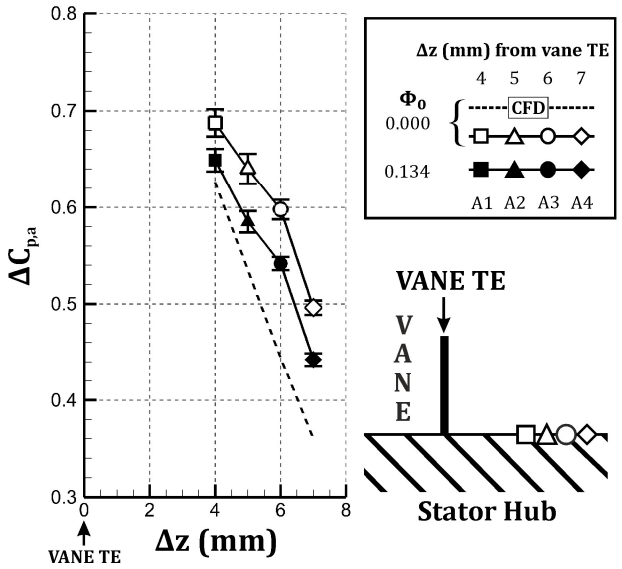

Figure 11 Axial decay in $\Delta C_{p,a}$ at Φ_0 = 0 and 0.134 (symbols – measured values; dashed line – CFD).

5.3 Stator hub pressure distributions

There are four sets of steady pressure taps distributed over one NGV pitch on the stator hub. Each set is circumferentially separated by 90° and consist of 15 pressure taps of diameter 0.5 mm; the 15 taps span the NGV pitch of 15°. Figure 10 shows a schematic with one such set (A1) which is 4 mm axially downstream of the NGV trailing edge. The sets are distributed axially (1 mm separation) such that A4 is located 7 mm downstream of the NGV trailing edge. Figure 10a shows the circumferential distribution of nondimensional pressure, $C_{p,a}$ (defined in the nomenclature), at A1 for two rotational Reynolds numbers (with consistent flow coefficient and zero purge). The dotted line shows the CFD prediction at Re_ϕ = 7.2 x 10^5; the CFD predicts the peak location and $\Delta C_{p,a}$ well. Figure 10b shows the circumferential distributions of nondimensional pressure for the sets A1 to A4; a decay in the magnitude of $\Delta C_{p,a}$ is apparent with axial distance from the NGV trailing-edge.

Figure 11 presents the axial decay in $\Delta C_{p,a}$ for $\Phi_0 = 0$ and $\sim \Phi_{min}$. Symbols represent experimental results; the bars represent the computed uncertainty; the dotted line represents the CFD prediction. Despite the offset between CFD and experiment, the gradients are equal to within experimental error. The introduction of purge was observed to reduce, or *'spoil'*, $\Delta C_{p,a}$.

5.4 Swirl measurements in the wheel-space

Figure 12 presents measurements of the radial distribution of swirl ratio, β (see nomenclature), in the wheel-space. These tests were performed at $Re_\phi = 7.2 \times 10^5$, $C_F = 0.38$ and for three values of Φ_0. The measurement points for the total pressure in the wheel-space at ($z/S = 0.19$) are also shown in Fig. 12. For $\Phi_0 = 0$, there is no superposed flow and a core rotation $\beta \approx 0.41$ is observed for $r/b = 0.75$ which is consistent with Daily *et al.* [38].

Increasing the sealing flow caused a reduction in the core rotation as the wheel-space pressurised. These results are consistent with the Batchelor-type flow model for rotating cavities discussed in Section 2.2.

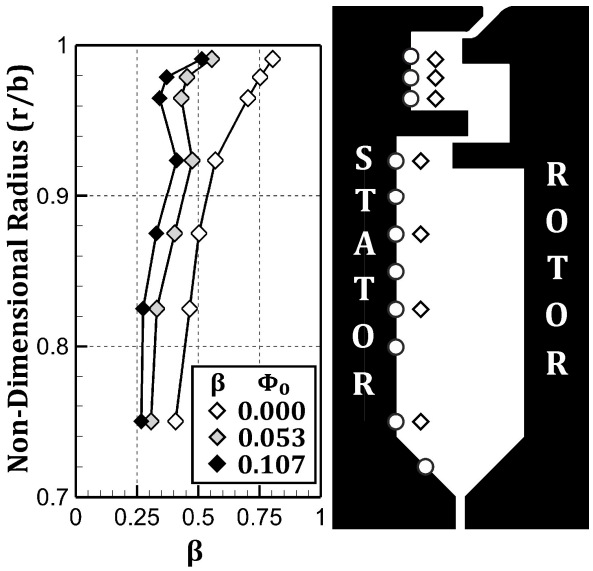

Figure 12 Effect of sealing flow rate on distribution of swirl ratio in the wheel-space.

5.5 Effectiveness measurements in the wheel-space

Measurements of effectiveness in the wheel-space for the double-clearance chute seal are shown in Fig. 14. All data were collected at a consistent flow coefficient of C_F = 0.38 at the operating conditions shown in Table 2. In all cases reported here the purge flow was 10% CO_2 in air (by volume).

Figure 13 presents the radial distribution of effectiveness in the wheel-space. The measurements were taken on the stator wall (circular symbols) and in the rotating core (diamond symbols) using sampling probes at z/S = 0.19. A silhouette of the seal is included alongside the figure; tap locations line up with the corresponding data in the plot. The external annulus flow is from left to right. The experiments were conducted at Re_ϕ = 7.2 x 10^5 for three values of Φ_0. Ingress occurred in all three cases. For both stator wall and core

measurements, ε_c increases with Φ_0 and the purge flow pressurises the wheel-space relative to the annulus.

A previous paper published by this research group (see [36]), for which a simpler double-clearance rim seal was tested, showed that the increase in sealing effectiveness from $\varepsilon_c = 0$ in the annulus across the outer seal is not as abrupt as Fig. 13 suggests, even at higher Φ_0. This is likely due to the relative rim-seal clearance between these studies. It is also noteworthy that in [36], the fluid in the outer seal was fully mixed (effectiveness showed negligible radial variation) whereas in Fig. 13, the effectiveness changes significantly on both the stator wall and in the core with radius. Interestingly, the rotating core measurements in the outer seal cavity indicate the maximum effectiveness occurs at the second of the three radial sampling points. This has been observed in CFD simulations for a similar double radial-clearance rim seal [39], where sealing flow is pumped by the rotor-side seal lip resulting in a local increase in effectiveness. As expected, the effectiveness significantly increases across the inner seal and into the inner wheel-space where the effectiveness is broadly invariant with radius. Hence, the fluid inside the inner wheel-space cavity is fully mixed. This is consistent with the fluid dynamics described in Section 2.2.

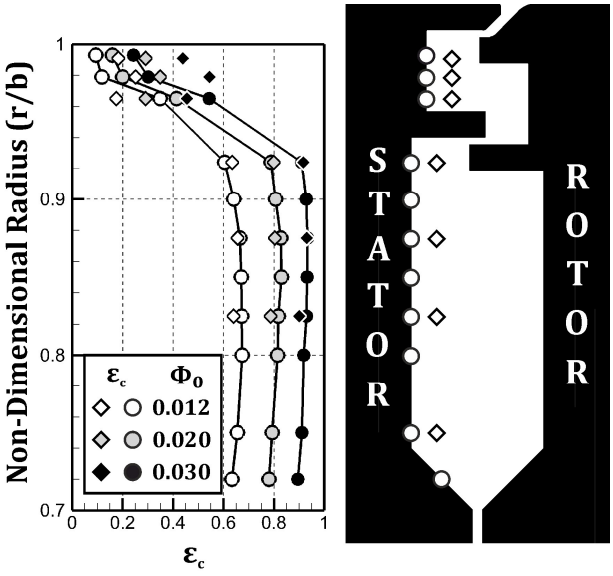

Figure 13 Effect of sealing flow rate on radial distribution of effectiveness in the wheel-space ($Re_\phi = 7.2 \times 10^5$ and $C_F = 0.38$) (circles – stator wall; diamonds – rotating core).

Figure 14 shows the variation of effectiveness with Φ_0 for the two operating conditions in Table 2. The measurements were taken on the stator wall in the inner and outer seal cavity (r/b = 0.9 and 0.979 respectively). The distribution of effectiveness is shown to be insensitive to rotational Reynolds number. ε_c increases with Φ_0 as the purge flow pressurises the wheel-space inhibiting ingress through the rim seal. Φ_{min} is defined as the value of Φ_0 at which $\varepsilon_c = 1$: for the inner seal cavity (at $r/b = 0.9$), $\Phi_{min} \approx 0.040$; for the outer seal cavity (at $r/b = 0.979$), $\Phi_{min} \approx 0.120$. Interestingly, a tenuous *kink* or inflexion is observed in the outer wheel-space between $0.02 < \Phi_0 < 0.05$. Similar, more distinct, behaviour has been reported by Horwood *et al.* [39]; the behaviour was associated with a magnification of low-frequency unsteadiness in the wheel-space. Boudet *et al.* [40], Gentilhomme *et al.* [41] and Clark *et al.* [42] also report a similar inflexion phenomenon but the authors do not discuss the driving mechanism. Further work by Hualca *et al.* [43] has shown that inflexion in the variation of effectiveness disappears when the blades are removed.

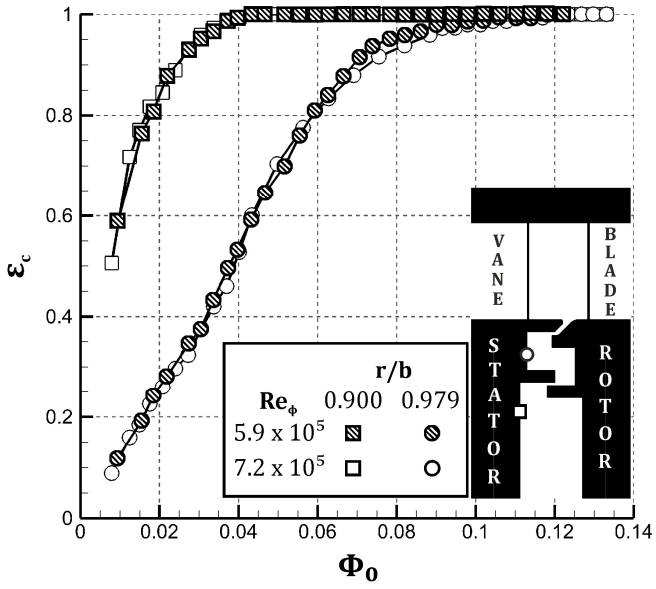

Figure 14 Variation of effectiveness with sealing flow rate at *r/b* = 0.9 and 0.979 in the wheel-space for $Re_\phi = 5.9 \times 10^5$ and 7.2×10^5 at $C_F = 0.38$ (lines are included for the reader's convenience)

6 OPTICAL MEASUREMENT CAPABILITIES

The primary objective for this new turbine facility is to provide expedient optical access for laser-based fluid measurement techniques. These techniques are to investigate the egress-mainstream interaction in the annulus, as discussed in Section 3.2. These techniques will reveal instantaneous and phase-averaged vector fields using VV - as demonstrated by [26] - and egress migration/diffusion with CO_2 PLIF - as demonstrated by [21]. This section presents the design of the opto-mechanics and requirement for PLIF in the LAR; the opto-mechanics for VV, which are simpler in design and involve borescopes which diverge the beam into a cone rather than a sheet will be discussed in a future publication. The borescopes for both optical methods were designed using detailed ray-tracing computational modelling and standard optical components. The design process used to develop the borescopes is the subject of another publication [44].

Figure 15 shows the opto-mechanical system that guides, collimates and introduces the laser light into the annulus between the stator and rotor. A section view of the system is shown in the top illustration; the borescope is positioned directly over the chute seal. In the bottom illustration, the borescope is positioned within a cavity inside the NGV which has a plano-convex N-BK7 window inset in a square recess; NBK-7 is transmissive to the light required for both VV and CO_2 PLIF. The external curve of the window matches the nominal shape of the NGV suction-surface to within 50 μm. It should be noted that the laser delivery systems shown in Fig. 15 are not coplanar and hence cannot be implemented in tandem.

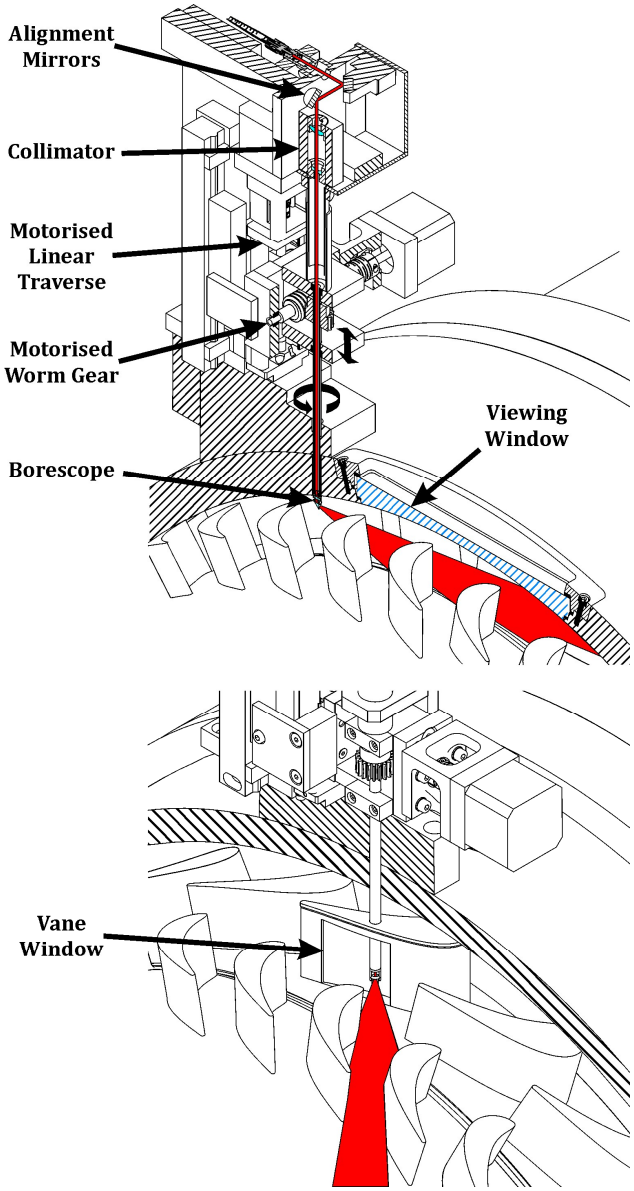

Figure 15 Laser delivery systems for the delivery of light upstream of the rotor. Top – borescopic delivery over the chute seal (Sapphire window shown in blue); Bottom – borescopic delivery from within the stator vane.

The system is designed to accommodate laser delivery via upstream mirrors or fibre-optics. Once introduced into the delivery system the laser beam takes two right angle turns via gold mirrors which can be adjusted/aligned with kinematic mounts. The collimator lenses are plano-convex and plano-concave lenses (Ø12.7 mm; f = 20 mm; N-BK7 and LC2067; Ø9 mm; f = -9 mm; N-SF11 respectively) and are arranged to form a Galilean-type beam

reducer. The purpose of the collimator is to provide control over the beam divergence and to reduce the beam diameter by a third. Tubed beam shielding is used to prevent exposure of the beam to the camera. During alignment, these would be replaced with a double pin hole alignment structure to ensure collinearity of the beam with the borescope objective.

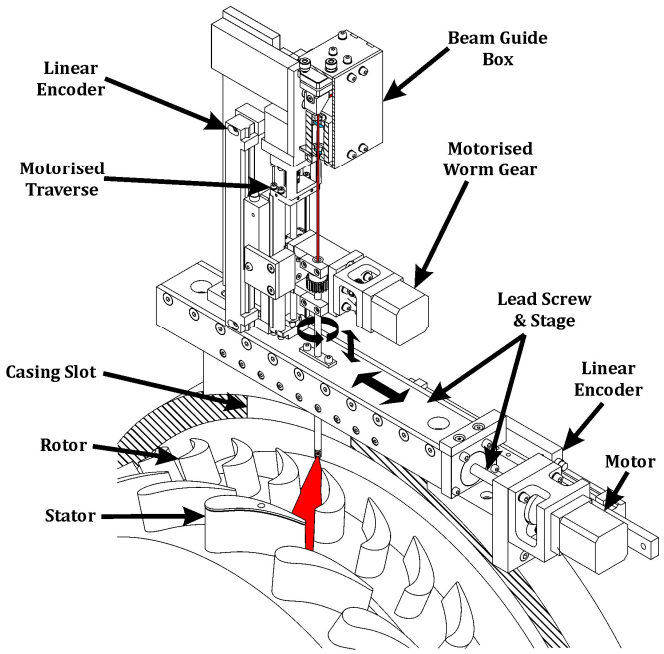

Figure 16 Laser delivery systems for the delivery of light downstream of the rotor.

In Fig. 15, the borescope is mechanically actuated by a motorised linear traverse which has position feedback from a linear encoder and a motorised rotating worm gear. The stepper motors have 200 steps per revolution with 32 micro-steps per step; the linear encoder is an optical-type slim linear scale with a precision of 5 μm; the linear motion actuator has a maximum stroke length of 40.9 mm. Figure 16 shows the borescopic system which introduces light from downstream of the rotor. This system is largely identical to that shown in Fig. 15 with the added capability of tangential actuation with position feedback from a larger linear encoder; a motor is used to drive the tangential motion. The tangential stage traverse is mobilised via two adjacent cross roller guides, not visible in Fig. 16. The smaller

motors were controlled with microstep drive units. The two borescopic systems are centrally controlled by an Arduino Mega 2560. The control program was written in BASCOM-AVR.

The viewing window is a 190 x 97 mm Sapphire window with a specified scratch/dig = 80/50 surface finish. The two axial edges of the window are notched such that the window sits against two tapered plastic pieces of shim which separate the window from the casing (Fig. 15 top LHS). The window is held/pressed in place by an aluminium boss which seals against the external surface of the Sapphire window with cork-infused rubber gaskets.

The infrared camera is an IRC800 camera and has a 100 mm focal length germanium lens. In the case of the LAR the appropriate field of view (governed by the window size and region of interest) is brought to focus with a 3/4 inch spacer added to the camera lens at an object-to-camera distance of 0.73 m. The infrared light is produced by second harmonic generation using a KTP frequency difference crystal. The crystal's input beams are provided by a Q-smart 850 Nd:YAG laser (1064 nm) and a nanosecond tuneable dye laser (pumped by 532 nm light from the Q-smart 850 laser with a frequency doubling crystal). The laser pulse and camera capture are synchronised in conjunction with the rotor phase. The rotor phase/clocking position is tracked by a visible light optical sensor.

7 CONCLUSIONS

This paper describes a new single-stage axial turbine research facility with expedient access for laser based fluid measurement techniques. The rig was designed to accommodate detailed instrumentation in a fluid dynamically scaled environment at a low Reynolds number. The rig is capable of providing information regarding the egress-mainstream interaction with VV and egress migration with CO_2 PLIF. Importantly, any rotor EWC can be inexpensively tested owing to the modular stator and interchangeable rotor blings.

This paper presents data for a double radial-clearance chute seal with a cylindrical rotor endwall. Future papers will examine the efficiency gains with optimised endwall designs in the presence of egress-mainstream interactions. Crucially, the laser based fluid measurement techniques will (in future studies) provide unprecedented insight into the fundamental fluid dynamics. The density ratio between the superposed purge flow and mainstream is variable from 1 to ≈ 1.5 (up to 100% CO_2 purge flow). This paper has presented results for 10% CO_2 purge flow (by volume) as a baseline case study.

The measured data presented for the baseline geometry agreed with predictions from a complementary CFD model within 10% of the presented scale ranges. The results were shown to be insensitive to changes in rotational Reynolds number. The introduction of purge flow had a negligible effect on the distributions of pressure coefficient over the NGVs. The distribution of pressure coefficient on the stator hub decays axially from the NGV trailing-edge. The fluid in the outer wheel-space was not fully mixed and demonstrated a difference in sealing effectiveness between the stator wall and the rotating core. The fluid dynamics in the inner seal cavity was consistent with the Batchelor-type flow model for rotating cavities.

ACKNOWLEDGEMENTS

The authors would like to thank Andrew Langley and Terrence Warder for their invaluable assistance in the construction of this new test facility. The authors would also like to thank Yan Sheng Li and Lars Hedlund (Siemens Industrial Turbomachinery Ltd.) for making a significant contribution to the rig design. The research described here was supported by the Engineering and Physical Sciences Research Council (EPSRC), through grant number EP/M026345/1, and Siemens Industrial Turbomachinery Ltd.

Data access: Due to confidentiality agreements with research collaborators, supporting data can only be made available to bona fide researchers subject to a

nondisclosure agreement. Details of how to request access are available at the University of Bath data archive website[1].

NOMENCLATURE

A_a	annulus cross sectional area (= $\pi r^2_{a,max}$-$\pi r^2_{a,min}$)
b	radius of seal (m)
C	axial chord of stator vane (m)
C_F	flow coefficient ($W/\Omega b$)
C_p	inlet pressure coeff. (= P / ½$\rho_a W^2$)
$C_{p,a}$	annulus hub pressure coeff. (= P_a-$\bar{P}_a$ / ½$\rho_a \Omega^2 b^2$)
$C_{p,n}$	stator vane pressure coeff. (= P-$P_{T,a}$ / ½$\rho_a \Omega^2 b^2$)
c	volumetric concentration of tracer gas (%)
c^*	mass concentration of tracer gas (%)
f	focal length (mm)
h	height (m)
M	vane exit Mach number
$\dot{m}$	mass flow rate (kg/s)
N	number of stator vanes
$\dot{n}$	mole flow rate (mol/s)
P	static pressure (= P_g + P_{ref}; Pa)
P_T	total pressure (Pa)
R_a	surface roughness (μm)
Re_w	axial Reynolds number in annulus based on radius (= $\rho W b/\mu$)
Re_ϕ	rotational Reynolds number (= $\rho \Omega b^2/\mu$)
$Re_{\phi,0}$	rotational Reynolds number (= $\rho_0 \Omega b^2/\mu_0$)

[1] http://dx.doi.org/10.15125/BATH-00116

R_u	universal gas constant
r	radius (m)
S	axial clearance between rotor and stator (m)
s_c	seal clearance (m)
T	temperature (K)
U	bulk mean radial seal velocity (= $\dot{m}_0/2\pi\rho_0 s_c b$)
V_r	radial component of velocity (m/s)
V_z	axial component of velocity (m/s)
V_ϕ	tangential component of velocity (m/s)
W	bulk mean axial velocity in annulus (= $\dot{m}_0/\rho_a A_a$)
X_i	arbitrary variable
y^+	nondimensional first cell height
z	axial coordinate (m)
β	swirl ratio (= $V_\phi/\Omega r$)
Δ	difference peak-to-trough
δX_i	uncertainty in X_i
ε	effectiveness
ε_c	concentration effectiveness
θ	nondimensional vane pitch (= $\phi/2\pi N$)
μ	dynamic viscosity (kg/m·s)
ρ	density (kg/m^3)
σ	turbulence intensity (% of local velocity)
Φ_0	non-dimensional sealing parameter (= $U/\Omega b$)
Φ_{min}	minimum value of Φ_0 to seal wheel-space
λ_T	turbulent flow parameter (= $C_{w,0}\,\mathrm{Re}_{\phi,0}^{-0.8}$)

ϕ azimuthal coordinate (rad)

Ω angular speed of rotating disc (rad/s)

Subscripts

a annulus

ax axial

B barometric

buffer wheel-space buffer cavity

g gauge (relative to reference value)

min minimum

max maximum

n nozzle guide vane

ov.,inner inner seal overlap

ov.,outer outer seal overlap

r radial

ref reference value

s stator surface

0 sealing flow

∞ core

REFERENCES

[1] Langston, L. S., 2001, "Secondary flows in axial turbines - a review," Ann. N. Y. Acad. Sci., 934(1), pp. 11-26.

[2] Harvey, N. W., Rose, M. G., Taylor, M. D., Shahpar, S., Hartland, J., and Gregory-Smith, D. G., 1999, "Non-axisymmetric turbine end wall design: Part I - three-dimensional linear design system," ASME J. Turbomach., 122(2), pp. 278-285.

[3] Rose, M. G., Harvey, N. W., Seaman, P., Newman, D. A., and McManus, D., 2001, "Improving the efficiency of the trent 500 HP turbine using non-axisymmetric end walls: Part II experimental validation," ASME Paper No. 2001-GT-0505.

[4] Harvey, N. W., Brennan, G., Newman, D. A., and Rose, M. G., 2002, "Improving turbine efficiency using non-axisymmetric end walls: Validation in the multi-row environment and with low aspect ratio blading," ASME Paper No. GT2002-30337.

[5] Schüpbach, P., Abhari, R. S., Rose, M. G., Germain, T., Raab, I., and Gier, J., 2010, "Improving efficiency of a high work turbine using nonaxisymmetric endwalls - Part II: time-resolved flow physics," ASME J. Turbomach., 132(2), p. 021008.

[6] Schüpbach, P., Abhari, R. S., Rose, M. G., Germain, T., Raab, I., and Gier, J., 2010, "Effects of suction and injection purge-flow on the secondary flow structures of a high-work turbine," ASME J. Turbomach., 132(2), p. 021021.

[7] Schüpbach, P., Abhari, R. S., Rose, M. G., and Gier, J., 2011, "Influence of rim seal purge flow on the performance of an endwall-profiled axial turbine," ASME J. Turbomach., 133(2), p. 021011.

[8] Regina, K., Kalfas, A. I., Abhari, R. S., Lohaus, A., Voelker, S., and auf dem Kampe, T., 2014, "Aerodynamic robustness of end wall contouring against rim seal purge flow," ASME Paper No. GT2014-26007.

[9] Wood, L. E., Jones, R. R., Pountney, O. J., Scobie, J. A., Rees, D. A. S., and Sangan, C. M., 2019, "A geometry generation framework for contoured endwalls," ASME Paper No. GT2019-90446.

[10] Takeishi, K., Matsuura, M., Aoki, S., and Sato, T., 1990, "An experimental study of heat transfer and film cooling on low aspect ratio turbine nozzles," ASME J. Turbomach., 112(3), pp. 488-496.

[11] Denton, J. D., 1993, "Loss mechanisms in turbomachines," ASME J. Turbomach., 115(4), pp. 621-656.

[12] Scobie, J. A., Sangan, C. M., Owen, M. J., and Lock, G. D., 2016, "Review of ingress in gas turbines," ASME J. Eng. Gas Turb. Power, 138(12), pp. 120801-120816.

[13] McLean, C., Camci, C., and Glezer, B., 2001, "Mainstream aerodynamic effects due to wheelspace coolant injection in a high-pressure turbine stage: Part I - aerodynamic measurements in the stationary frame," ASME Paper No. 2001-GT-0119.

[14] Paniagua, G., Dénos, R., and Almeida, S., 2004, "Effect of the hub endwall cavity flow on the flow-field of a transonic high-pressure turbine," ASME J. Turbomach., 126(4), pp. 578-586.

[15] Ong, J., Miller, R. J., and Uchida, S., 2012, "The effect of coolant injection on the endwall flow of a high pressure turbine," ASME J. Turbomach., 134(5), pp. 051003-051008.

[16] Porreca, L., Yun, Y. I., Kalfas, A. I., Song, S. J., and Abhari, R. S., 2006, "Investigation of 3D unsteady flows in a two stage shrouded axial turbine using stereoscopic PIV and FRAP: Part I - interstage flow interactions," ASME Paper No. GT2006-90752.

[17] Bryanston-Cross, P. J., Chana, K. S., and Healey, N., 1997, "Particle image velocimetry measurements from the stator-rotor interaction region of a high pressure transonic turbine stage at the DERA isentropic light piston facility," AGARD PEP Symposium on “Advanced Non-Intrusive Instrumentation for Propulsion Engines".

[18] Yun, Y. I., Porreca, L., Kalfas, A. I., Song, S. J., and Abhari, R. S., 2006, "Investigation of 3D unsteady flows in a two-stage shrouded axial turbine using stereoscopic PIV and FRAP: Part II - kinematics of shroud cavity flow," ASME Paper No. GT2006-91020.

[19] Balzani, N., Scarano, F., Riethmuller, M. L., and Breugelmans, F. A. E., 2000, "Experimental investigation of the blade-to-blade flow in a compressor rotor by digital particle image velocimetry," ASME J. Turbomach., 122(4), pp. 743-750.

[20] Kegalj, M., and Schiffer, H. P., 2009, "Endoscopic PIV measurements in a low pressure turbine rig," Exp. Fluids, 47(4-5), pp. 689-705.

[21] Kirby, B. J., and Hanson, B. K., 2000, "Imaging of CO and CO_2 using infrared planar laser-induced fluorescence," Proc. Comb. Inst., 28(1), pp. 253-259.

[22] Kirby, B. J., 2001, "Infrared planar laser-induced fluorescence imaging and applications to imaging of carbon monoxide and carbon dioxide," PhD Thesis, Stanford University.

[23] Crimaldi, J. P., 2008, "Planar laser induced fluorescence in aqueous flows," Exp. Fluids, 44(6), pp. 851-863.

[24] Zetterberg, J., Blomberg, S., Gustafson, J., Sun, Z. W., Li, Z. S., Lundgren, E., and Aldén, M., 2012, "An *in situ* set up for the detection of CO_2 from catalytic CO oxidation by using planar laser-induced fluorescence," Rev. Sci. Instrum., 83(5), p. 053104.

[25] Pu, J., Wang, J., Ma, S., and Wu, X., 2015, "An experimental investigation of geometric effect of upstream converging slot-hole on end-wall film cooling and secondary vortex characteristics," Exp. Therm. Fluid Sci., 69, pp. 58-72.

[26] Carvalho Figueiredo, A. J., Jones, R. R., Pountney, O. J., Scobie, J. A., Lock, G. D., Sangan, C. M., and Cleaver, D. J., 2018, "Volumetric velocimetry measurements of film cooling jets," ASME J. Eng. Gas Turb. Power, 141(3), pp. 031021-031013.

[27] Stellmacher, M., and Obermayer, K., 2000, "A new particle tracking algorithm based on deterministic annealing and alternative distance measures," Exp. Fluids, 28(6), pp. 506-518.

[28] Woisetschläger, J., and Göttlich, E., 2007, "Recent applications of particle image velocimetry to flow research in thermal turbomachinery," Particle Image Velocimetry, Springer, pp. 311-331.

[29] Ceyhan, I., dHoop, E. M., Guenette, G. R., Epstein, A. H., and Bryanston-Cross, P. J., 1998, "Optical instrumentation for temperature and velocity measurements in rig turbines," AGARD PEP Symposium on “Advanced Non-Intrusive Instrumentation for Propulsion Engines".

[30] Sell, M., Schlienger, J., Pfau, A., Treiber, M., and Abhari, R. S., 2001, "The 2-Stage Axial Turbine Test Facility “LISA”," (78507), p. V001T003A076.

[31] Sovran, G., and Klomp, E. D., 1967, "Experimentally determined optimum geometries for rectilinear diffusers with rectangular, conical or annular cross-section," Fluid Dynamics of Internal Flow, Elsevier, New York, pp. 270-319.

[32] Stern, F., Wilson, R. V., Coleman, H. W., and Paterson, E. G., 2001, "Comprehensive approach to verification and validation of CFD simulations - Part 1: methodology and procedures," ASME J. Fluids Eng., 123(4), pp. 793-802.

[33] Roach, P. E., 1987, "The generation of nearly isotropic turbulence by means of grids," Int. J. Heat Fluid Flow, 8(2), pp. 82-92.

[34] Levenspiel, O., 1958, "Longitudinal Mixing of Fluids Flowing in Circular Pipes," Industrial & Engineering Chemistry, 50(3), pp. 343-346.

[35] Buddenberg, J. W., and Wilke, C. R., 1949, "Calculation of gas mixture viscosities," Ind. & Eng. Chem., 41(7), pp. 1345-1347.

[36] Patinios, M., Scobie, J. A., Sangan, C. M., Owen, M. J., and Lock, G. D., 2016, "Measurements and modeling of ingress in a new 1.5-stage turbine research facility," ASME J. Eng. Gas Turb. Power, 139(1), pp. 012603-012612.

[37] Schreiner, B. D., Li, Y. S., Wilson, M., and Sangan, C. M., "Computational investigation of purge-mainstream interaction in gas turbines," To be submitted to ASME J. Turbomach.

[38] Daily, J. W., Ernst, W. D., and Asbedian, V. V., 1964, "Enclosed rotating disks with superposed throughflow," Dept of Civil Eng., Hydrodyn. Lab. MIT Rep. No.64.

[39] Horwood, J. T. M., Hualca, F. P., Scobie, J. A., Wilson, M., Sangan, C. M., and Lock, G. D., 2018, "Experimental and computational investigation of flow instabilities in turbine rim seals," ASME J. Eng. Gas Turb. Power, 141(1), pp. 011028-011012.

[40] Boudet, J., Autef, V. N. D., Chew, J. W., Hills, N. J., and Gentilhomme, O., 2005, "Numerical simulation of rim seal flows in axial turbines," Aeronaut. J., 109(1098), pp. 373-383.

[41] Gentilhomme, O., Hills, N. J., Turner, A. B., and Chew, J. W., 2003, "Measurement and analysis of ingestion through a turbine rim seal," ASME J. Turbomach., 125(3), pp. 505-512.

[42] Clark, K., Barringer, M., Johnson, D., Thole, K., Grover, E., and Robak, C., 2018, "Effects of purge flow configuration on sealing effectiveness in a rotor–stator cavity," ASME J. Eng. Gas Turb. Power, 140(11), p. 112502.

[43] Hualca, F. P., Horwood, J. T. M., Scobie, J. A., Sangan, C. M., and Lock, G. D., 2019, "The effect of vanes and blades on ingress in gas turbines," ASME Paper No. GT2019-90987.

[44] Carvalho Figueiredo, A. J., Jones, R. R., Sangan, C. M., and Cleaver, D. J., "A borescope design tool for laser measurements in fluids," To be submitted to Opt. Lasers Eng.

[45] Moffat, R. J., 1988, "Describing the uncertainties in experimental results," Exp. Therm. Fluid Sci., 1(1), pp. 3-17.

APPENDIX: UNCERTAINTY ANALYSIS

Uncertainty analysis was performed as per [45]. The uncertainty results and instrumentation specifications are tabulated in Tables 3 and 4 respectively. For brevity, the analysis is presented for the sealing flow parameter defined as:

$$\Phi_0 = \frac{\dot{m}_0}{2\pi\rho_0 s_c \Omega b^2} \tag{A.1}$$

where

$$\dot{m}_0 = \dot{m}_{0,air} + \dot{m}_{0,CO2} \tag{A.2}$$

The density of the purge flow is calculated by:

$$\rho_0 = \frac{(P_0+P_B)\dot{m}_0}{R_u \dot{n}_0 T_0} \tag{A.3}$$

where the total mole flow rate is:

$$\dot{n}_0 = \left(\frac{\dot{m}_{0,air}}{M_{air}} + \frac{\dot{m}_{0,CO2}}{M_{CO2}}\right) \tag{A.4}$$

The uncertainty is then:

$$\left(\frac{\delta\Phi_0}{\Phi_0}\right)^2 = \left(\frac{M_{CO2}}{\dot{n}_0}\delta\dot{m}_{0,air}\right)^2 + \left(\frac{M_{air}}{\dot{n}_0}\delta\dot{m}_{0,CO2}\right)^2 + \left(\frac{\delta P_0}{P_0+P_B}\right)^2 + \left(\frac{\delta P_B}{P_0+P_B}\right)^2 + \left(\frac{\delta T_0}{T_0}\right)^2 + \left(\frac{\delta\Omega}{\Omega}\right)^2 \tag{A.5}$$

where the error on *b* is ignored.

$\delta\Phi_0/\Phi_0$	$\delta\rho_0/\rho_0$	$\delta\varepsilon_c/\varepsilon_c$	$\delta C_p/C_p$
$\pm$ 0.2%	$\pm$ 0.21%	$\pm$ 3%	$\pm$ 3.7%

Table 3 Estimated measurement uncertainty

X_i	δX_i	Scale Range (Units)	Instrument
P_g	$\pm$ 2 Pa	2 kPa	0.3 PSI-D-HGRADE-MV
P_a, P_0	$\pm$ 35 Pa	35 kPa	5 PSI-D-HGRADE-MV
P_B	$\pm$ 50 Pa	75 to 125 kPa	Pi642P-.75-1.25BARA-0.1
T_a, T_0	$\pm$ 0.5 K	3 to 1530 K	K-type Thermocouple
Ω	$\pm$ 1 rpm	6000 rpm	34kW AC Dynamometer
$\dot{m}_{0,CO2}$	$\pm$ 0.8 % Read, $\pm$ 0.2 % Full Scale	3.0 kg/minute	MCR-1500SLPM-D
$\dot{m}_{0,air}$	$\pm$ 1 % Read, $\pm$ 0.5 % Full Scale	2.9 kg/minute	F-206AI-ABD-00-V
$\dot{m}_a$	$\pm$ 1 % Read, $\pm$ 0.5 % Full Scale	1.7 kg/s	780S-NAA-F9-EN2-P2-V3-DD-0
c_s, c_a, c_0	$\pm$ 0.1 % Full Scale	100 % CO_2	9120MG Multi Gas Analyser

Table 4 Precision and specifications of the instrumentation